Volume and Heat Budgets in the Coastal California Current System: Means, Annual Cycles, and Interannual Anomalies of 2014–16

KATHERINE D. ZABA, DANIEL L. RUDNICK, BRUCE D. CORNUELLE, GANESH GOPALAKRISHNAN, AND MATTHEW R. MAZLOFF

Scripps Institution of Oceanography, La Jolla, California

ABSTRACT

The data-assimilating California State Estimate (CASE) enables the explicit evaluation of spatiotemporally varying volume and heat budgets in the coastal California Current System (CCS). An analysis of over 10 years of CASE model output (2007–17) diagnoses the physical drivers of the CCS mean state, annual cycles, and the 2014–16 temperature anomalies associated with a marine heat wave and an El Niño event. The largest terms in the mean mixed layer (from −50 to 0 m) volume budgets are upward vertical transport at the coast and offshore-flowing ageostrophic Ekman transport at the surface, the two branches of the coastal upwelling overturning cell. Contributions from onshore geostrophic flow in the Southern California Bight and alongshore geostrophic convergence in the central CCS balance the mean volume budgets. The depth-dependent annual cycle of vertical velocity exhibits the strongest upward velocity between −40- and −30-m depth in April. Interannual volume budgets show that over 50% of the 2013.5–16.5 time period experienced downwelling anomalies, which were balanced predominantly by alongshore transport convergence and, less often, by onshore transport anomalies. Mixed layer temperature anomalies persisted for the entirety of 2014–16, reaching a maximum of +3° in October 2015. The mixed layer heat budget shows that intermittent high air–sea heat flux anomalies and alongshore and vertical heat advection anomalies all contributed to warming during 2014–16. A subsurface (from −210 to −100 m) heat budget reveals that in September 2015 anomalous poleward heat advection into the Southern California Bight by the California Undercurrent caused deeper warming during the 2015/16 El Niño.

1. Introduction

During 2014–16 two sequential Pacific Ocean climate events dramatically altered the physical state of the California Current System (CCS). Local temperature anomalies associated with a marine heat wave (MHW) and an equatorial El Niño event peaked at the turn of the years 2014/15 and 2015/16, respectively. We use numerical output from the California State Estimate (CASE; Zaba et al. 2018) to calculate coastal volume and heat budgets with the goal of diagnosing which physical mechanisms caused the circulation and heat content anomalies during 2014–16. Budgets of the mean state and annual cycle are calculated first, revealing circulation features that we believe to be previously undescribed. These include new estimates of the ageostrophic wind-driven Ekman transport, the three-dimensional volume balance of the upwelling overturning cell, and the spatial

variability of the vertical velocity annual cycle. The interannual mixed layer budgets (from −50 to 0 m) consist of time-varying anomalous heating contributions from surface heat flux, downwelling, and lateral heat advection. Subsurface (from −210 to −100 m) anomalous poleward heat advection occurred in the Southern California Bight in autumn of 2015. The analysis reveals that no single process can account for the 2014–16 anomalies in the CCS; rather, they are the result of multiple mechanisms represented by the volume and heat budgets occurring intermittently at different times and locations throughout the region.

Mean CCS horizontal circulation over the upper 500 m includes the equatorward, near-surface California Current in the offshore region; the poleward, subsurface California Undercurrent (CU) nearshore (Lynn and Simpson 1987; Rudnick et al. 2017a); and Ekman transport in a thin surface layer flowing offshore, normal to the equatorward alongshore winds (Chereskin 1995) (Fig. 1). A previous mass budget calculation in the

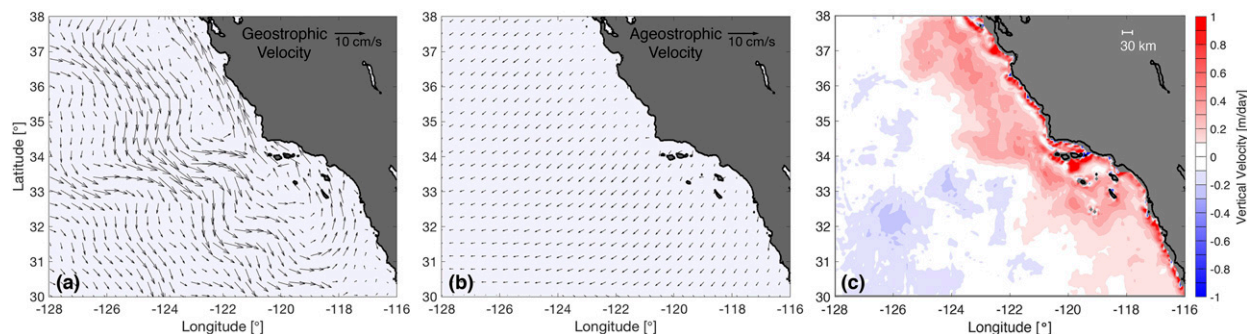*Corresponding author:* Katherine Zaba, kzaba@ucsd.edu

FIG. 1. Plan view of 2007–13 mean circulation decomposed into (a) geostrophic, (b) ageostrophic, and (c) vertical velocity. The horizontal velocities in (a) and (b) are vertically averaged over −50–0-m depth, subsambled at $\frac{3}{8}°$ resolution (~48 km), and plotted in centimeters per second according to the scale vector in the upper right. Vertical velocities across −50 m in (c) are plotted in meters per day according to the color bar, where red is upward and blue is downward. A scale bar for horizontal distance is in the upper-right corner of (c).

southern CCS by Bograd et al. (2001) showed a close balance between geostrophic convergence and Ekman divergence over the upper 500 m. At shallower depths, vertical upwelling velocities become relevant in the mass balance. Equatorward winds drive local upwelling by two processes: first, horizontal mass divergence at the coast due to offshore Ekman transport and, second, Ekman suction offshore due to a positive wind stress curl (Rykaczewski and Checkley 2008). A wind-driven cross-shore upwelling overturning cell exists in the coastal upwelling zone (Davis 2010; Nelson 1977).

The CCS region is one of net downward air–sea heat flux Q_o, estimated by Bograd et al. (2001) to have a mean value of 86 W m^{-2} in the southern CCS. Advective heat export becomes important toward the coast and is primarily due to offshore Ekman transport, though alongshore geostrophic transport, and to a lesser degree, cross-shore geostrophic transport and eddy transport can contribute as well (Edwards and Kelly 2007). Heat storage rates peak in the summer, when Q_o and advective heat export do not balance.

The unusual 2014/15 MHW was a large-scale warming that spanned the eastern North Pacific Ocean basin from the Gulf of Alaska to Baja California (Bond et al. 2015; Di Lorenzo and Mantua 2016; Gentemann et al. 2017; Robinson 2016). The temperature anomalies associated with the MHW varied in phase and amplitude along the North American coastline. In the southern and central CCS, the MHW caused a surface-intensified warm pool, high stratification, and thermocline deepening due to a local increase in surface heat flux and decrease in upwelling winds (Robinson 2016; Zaba and Rudnick 2016). Model results from Chao et al. (2017) attributed the warming over December 2013–March 2014 in the central CCS to anomalous downward air–sea heat fluxes and onshore heat advection. They concluded that ocean entrainment anomalies were not a primary driver of the

warming. However, their budget volume extended down to −100-m depth, well below the depth of maximum upwelling and therefore unable to capture its most significant variability. A mixed layer energy budget by Myers et al. (2018) found that anomalous sea surface temperature warming off Baja California was due to reduced cloud coverage and a consequent increase in downwelling solar radiation. The MHW had major impacts on the CCS ecosystem, including a deepening of the subsurface chlorophyll-a maximum (Zaba and Rudnick 2016) and a widespread *pseudo-nitzschia* bloom (Cavole et al. 2016; McCabe et al. 2016).

On the tail of the 2014/15 MHW was the 2015/16 El Niño, which was classified as a strong event at the equator. In the CCS, the event caused isopycnals to deepen further (Jacox et al. 2016) and, in some locations, the warm anomaly penetrated deeper resulting in the warmest water observed off southern California in the instrumental record (Zaba et al. 2018). The heat budget analysis from Chao et al. (2017) attributed the warming over December 2015–March 2016 to anomalous alongshore advection from the south. Frischknecht et al. (2017) attributed the onset of regional El Niño anomalies to remote forcing via poleward-propagating coastally trapped waves, which depress the thermocline. Somewhat surprisingly, equatorward upwelling-favorable winds developed in autumn of 2015, possibly damping what could have been much stronger regional El Niño effects (Frischknecht et al. 2017; Jacox et al. 2016).

This paper builds on the Zaba et al. (2018) evaluation of CASE relative to the California Underwater Glider Network (CUGN) climatology data product (Rudnick et al. 2017a,b). For key observed physical features of the CCS mean state, annual cycles, and interannual variability, the comparative analysis showed CASE–CUGN correlation coefficients greater than 0.8. Along California Cooperative Oceanic Fisheries Investigations (CalCOFI)

line 90 in the Southern California Bight, the −50-m temperature anomaly from the annual cycle peaked at the turn of 2014/15 (MHW) and 2015/16 (El Niño). Along CalCOFI lines 66.7 and 80, the −50-m temperature anomaly was elevated for the entire 2014–16 period without a notable distinction between the events. Sustained downwelling anomalies persisted throughout the 2014–16 period along all lines, peaking during the 2015/16 El Niño. An isopycnal salinity anomaly also co-occurred with the peak of the 2015/16 El Niño, suggesting anomalous advection from the south. CASE's ability to reproduce these signals motivates its use in investigating the forcing mechanisms that drove them.

The primary objective of this study is to diagnose the drivers of the CCS mean state, annual cycles, and 2014–16 temperature anomalies. We calculate volume and heat budgets, both surface (from −50 to 0 m) and subsurface (from −210 to −100 m), within two fixed coastal boxes to address hypotheses about the relevant forcing mechanisms. For the interannual anomalies, we construct a timeline of the relative contributions of all heating mechanisms: air–sea heat fluxes, horizontal and vertical heat advection, mixing. We find that all mechanisms were important, depending on the time and location being examined. The remainder of this paper is organized as follows: section 2a describes the CASE, and section 2b describes the budget calculation method; sections 3a and 3b detail the results from the volume and heat budget calculations, respectively; and section 4 summarizes and discusses the results.

2. Data and methods

a. Numerical state estimate

CASE is the optimized solution from a regional implementation of the Massachusetts Institute of Technology general circulation model (MITgcm; Marshall et al. 1997)–Estimating the Circulation and Climate of the Ocean (ECCO; Stammer et al. 2002) four-dimensional variational (4DVAR) assimilation system. The model domain extends from 27° to 40°N and from 130° to 114°W, and it is integrated on a (1/16)° × (1/16)° (~8 km) spherical polar grid, with 72 vertical z levels. It assimilates a variety of regional to global remote and in situ datasets, including satellite sea surface height and temperature, Argo profiles, CUGN glider profiles, and high-resolution expendable bathythermograph (XBT) profiles. The version of CASE used here consists of 41 sequential, nonoverlapping 3-month state estimates covering 1 January 2007–31 March 2017. Constrained by governing physical equations and assimilated observations, CASE is a realistic and dynamically consistent ocean state estimate with closed

physical budgets over each 3-month assimilation window. More information about CASE, as well as an assessment of its strengths and its biases, is detailed in Zaba et al. (2018).

Successive state estimates are calculated independently, with the assimilation adjusting first-guess initial and open-ocean boundary conditions from the Hybrid Coordinate Ocean Model (HYCOM) global (1/12)° daily analysis (Chassignet et al. 2007), as well as the time-varying prescribed atmospheric state from which air–sea fluxes are calculated using the Large and Pond (1981) bulk formula. Balanced budgets are maintained over each 3-month assimilation window but discontinuities in heat content may exist between the end of one window and the start of the next. Increments for these discontinuities are needed to compensate for model errors, input errors, or uncontrollable intrinsic oceanic variability. In CASE, the increments are thought to arise primarily from integrated biases in shortwave radiation estimates from the National Centers for Environmental Prediction–National Center for Atmospheric Research reanalysis (Kalnay et al. 1996) used as the atmospheric forcing in CASE. The hypothesis is that the reanalysis does not capture the effect of low-level clouds over the coastal CCS and estimates excessive shortwave radiative fluxes into the ocean. The increment absolute values are largest early in the assimilation, especially before 2010, suggesting this issue is improved in later years. Though we hypothesize the bias arises from excessive radiative heating, each state estimate is only of 3-month duration allowing ambiguity in the optimization between initial conditions and atmospheric forcing errors. With this in mind, we account for the initial condition increments by attributing the adjustments to an atmospheric heat flux bias as explained in section 2b(2).

Following the method of the CUGN climatology (Rudnick et al. 2017a,b) and CUGN–CASE evaluation (Zaba et al. 2018), interannual anomalies are defined relative to mean and annual cycle fields calculated over the base period 2007–13 (inclusive). At each model grid point, a least squares fit of seven temporally varying functions (a constant, and the first three annual harmonics of sine and cosine) produces the mean and an annual cycle evaluated at every day of the year. The difference between the gridded CASE output and the derived annual cycle is the interannual anomaly. This calculation is applied to all relevant state variables and diagnostic variables.

b. Budget calculations

Volume and heat budget terms from CASE are diagnosed in an integrated box budget sense. We use existing CalCOFI geometry (Eber and Hewitt 1979) to define two boxes: NBox and SBox, shown in Fig. 2.
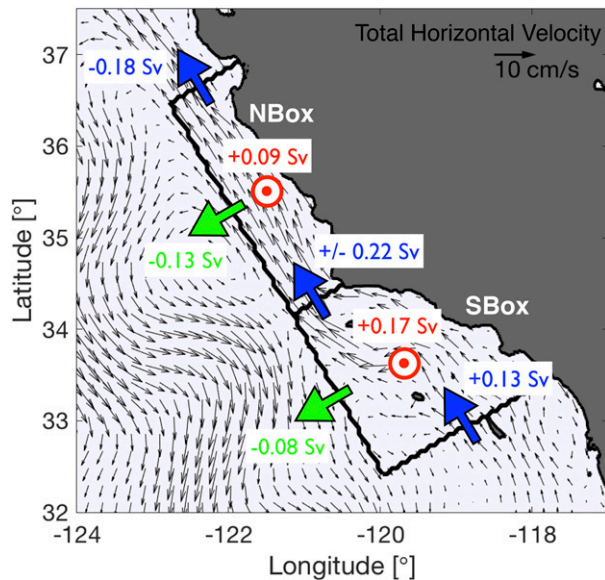
FIG. 2. Plan view of 2007–13 mean mixed layer volume budgets of NBox and SBox, the perimeters of which are the thick black lines. Thin black arrows represent the horizontal velocity field vertically averaged over −50–0-m depth, subsampled at $(3/16)°$ resolution (~24 km), and plotted in centimeters per second, according to scale vector in the upper right. Labeled colored arrows represent integrated volume transport in Sverdrups across the box walls: U_{west} (green), V_{north} and V_{south} (blue), and W_{-50m} (red), as in Eq. (4) with $z_1 = -50$ m.

NBox is bounded by CalCOFI lines 66.7 and 80, and SBox is bounded by lines 80 and 90. Both boxes are bound by the coastline to the east and CalCOFI station 60 to the west, which is located approximately 96, 71, and 239 km offshore along lines 66.7, 80, and 90, respectively. Consistent with the CalCOFI geometry, we calculate budgets in a rotated reference frame. Hereinafter, u and v refer to across-shore and alongshore velocity components, respectively, where the rotation angle, θ, is 30° north of west.

NBox and SBox encompass distinct geographic regions, the central CCS and Southern California Bight (SCB), with different physical characteristics. Furthermore, we examine these box budgets at different depths in the water column. Our shallow, mixed layer box is bound by −50- and 0-m depths, because previous studies have shown that −50 m is the mean depth of the top of the thermocline in this region (Rudnick et al. 2017a; Zaba et al. 2018). Our subsurface box is bound by −210- and −100-m depths because those isobars encompass the 26.0 kg m^{-3} isopycnal and the deeper portion of the 2015/16 temperature anomaly (Zaba et al. 2018).

1) VOLUME BUDGET

For the volume budget we start with the equation for the conservation of mass:

$$\nabla \cdot \mathbf{u} = 0, \qquad (1)$$

where $\nabla\cdot$ is the divergence vector operator and $\mathbf{u}$ is the three-dimensional velocity vector. Applying a volume integral and the divergence theorem to Eq. (1) yields

$$\oiint_S \mathbf{u} \cdot \hat{\mathbf{n}} \, dS = 0, \qquad (2)$$

where S denotes the surface of the volume and $\hat{\mathbf{n}}$ is the outward-facing normal unit vector on S. For the NBox and SBox volumes (Fig. 2), the boxes are laterally bound by a west wall, a north wall, a south wall, and the coastline on the east, across which there is no exchange of mass or heat. The box corners are the following coordinates x_{SW} (southwest), x_{SE} (southeast), x_{NW} (northwest), and x_{NE} (northeast). The dimension z is defined as positive upward, and the volumes' vertical bounds are depths z_1 and z_2, where z_i is negative and $z_1 < z_2$. In this geometry, the volume integral of the mass conservation equation is

$$\underbrace{\int_{x_{SW}}^{x_{NW}} \int_{z_1}^{z_2} u \, dz \, dl}_{U_{west}} + \underbrace{\int_{x_{SW}}^{x_{SE}} \int_{z_1}^{z_2} v \, dz \, dl}_{V_{south}} - \underbrace{\int_{x_{NW}}^{x_{NE}} \int_{z_1}^{z_2} v \, dz \, dl}_{V_{north}}$$
$$+ \underbrace{\int_A \left(w_{z_1} - w_{z_2}\right) dx \, dy}_{W} = 0, \qquad (3)$$

where u, v, and w are the across-shore, alongshore, and vertical velocity components, respectively; l is the box perimeter as defined by the aforementioned box corners and displayed in Fig. 2; and A is the surface area bound by the box perimeter. The terms of Eq. (3) are cross-shore transport across the west wall (U_{west}), alongshore transport across the south wall (V_{south}), alongshore transport across the north wall (V_{north}), and vertical transport (W), all in units of meters cubed per second, or Sverdrups (Sv) when multiplied by 10^{-6} Sv s m^{-3} (i.e., 1 Sv $\equiv 10^6$ m^3 s^{-1}). Breaking the convention described in Eq. (2), positive transport values in Eq. (3) are defined as into the boxes, so as to be able to describe upward vertical transports across the bottom wall or lateral and vertical volume convergences as "into the box." Vertical velocity w at the ocean surface is zero, so for boxes with an upper vertical boundary of $z_2 = 0$ and a lower vertical boundary of $z = z_1$, Eq. (3) becomes

$$\underbrace{\int_{x_{SW}}^{x_{NW}} \int_{z_1}^{0} u \, dz \, dl}_{U_{west}} + \underbrace{\int_{x_{SW}}^{x_{SE}} \int_{z_1}^{0} v \, dz \, dl}_{V_{south}} - \underbrace{\int_{x_{NW}}^{x_{NE}} \int_{z_1}^{0} v \, dz \, dl}_{V_{north}}$$
$$+ \underbrace{\int_A w_{z_1} \, dx \, dy}_{W} = 0. \qquad (4)$$

In MITgcm the volume between $z = 0$ and the free surface, η, is nonzero. However, its contribution is negligible in our vertical integrals over 50 m or more; therefore, we exclude it from Eq. (4) and all subsequent vertically integrated equations.

The horizontal velocity fields are decomposed into geostrophic and ageostrophic components (i.e., $u = u_g + u_a$ and $v = v_g + v_a$). We define the geostrophic velocity components to be

$$u_g = -\frac{1}{\rho_0 f}\frac{\partial p}{\partial y} \quad \text{and} \quad v_g = \frac{1}{\rho_0 f}\frac{\partial p}{\partial x}, \quad (5)$$

where p is anomaly from hydrostatic pressure. Defining the ageostrophic velocities to have no pressure signature, we calculate the ageostrophic velocity components u_a and v_a as the residual between the model velocity fields and the derived geostrophic velocity (i.e., $u_a = u - u_g$ and $v_a = v - v_g$). Then Eq. (3) can be decomposed into

$$\underbrace{\int_{x_{\mathrm{SW}}}^{x_{\mathrm{NW}}}\int_{z_1}^{z_2}(u_g + u_a)\,dz\,dl}_{U_{g,\mathrm{west}}+U_{a,\mathrm{west}}} + \underbrace{\int_{x_{\mathrm{SW}}}^{x_{\mathrm{SE}}}\int_{z_1}^{z_2}(v_g + v_a)\,dz\,dl}_{V_{g,\mathrm{south}}+V_{a,\mathrm{south}}}$$

$$\underbrace{-\int_{x_{\mathrm{NW}}}^{x_{\mathrm{NE}}}\int_{z_1}^{z_2}(v_g + v_a)\,dz\,dl}_{V_{g,\mathrm{north}}+V_{a,\mathrm{north}}} + \underbrace{\int_A\left(w_{z_1} - w_{z_2}\right)dx\,dy}_{W} = 0, \quad (6)$$

where the terms are geostrophic and ageostrophic cross-shore transport across the west wall ($U_{g,\mathrm{west}}$ and $U_{a,\mathrm{west}}$), geostrophic and ageostrophic alongshore transport across the south wall ($V_{g,\mathrm{south}}$ and $V_{a,\mathrm{south}}$), and geostrophic and ageostrophic alongshore transport across the north wall ($V_{g,\mathrm{north}}$ and $V_{a,\mathrm{north}}$), and the vertical transport remains the same as in Eq. (3).

2) HEAT BUDGET

By design, CASE satisfies the heat conservation equation at every grid point:

$$\underbrace{\rho_o c_p \frac{\partial T}{\partial t}}_{\text{temperature tendency}} = \underbrace{\frac{\partial Q}{\partial z}}_{\text{air-sea heat flux}} - \rho_o c_p \left[\underbrace{\mathbf{u}\cdot\nabla T}_{\text{heat advection}} \right.$$

$$\left. - \left(\underbrace{\kappa_H \nabla_H^2 T + \kappa_Z \frac{\partial^2 T}{\partial z^2} + K_T^{\mathrm{turb}}}_{\text{heat diffusion}}\right)\right], \quad (7)$$

where T is potential temperature, ρ_0 is a constant density (1027 kg m^{-3}), c_p is the specific heat capacity of seawater (3994 J kg^{-1} °C^{-1}), Q is the net air–sea heat flux (where downward into the ocean is positive), κ_H and κ_Z are the horizontal and vertical diffusivity, ∇_H is the horizontal divergence operator, and K_T^{turb} is the K-profile parameterization (KPP) turbulent vertical diffusion. Equation (7), in units of watts per meter cubed, is adapted and rearranged from Tamsitt et al. (2016), who conducted a heat budget analysis of the Southern Ocean State Estimate (SOSE), another regional, data-assimilating implementation of the MITgcm-ECCO 4DVAR assimilation system. The CASE diagnostic fields allow for the explicit evaluation of all terms at every grid point and time step. As in Tamsitt et al. (2016), the vertical redistribution of incoming solar radiation [contributing to the air–sea heat flux term of Eq. (7)] is based on an assumption of exponential attenuation with depth. In CASE, the water type is Jerlov IA, where 62% of the shortwave radiation attenuates with an e-folding scale of 0.6 m and the remainder (38%) with an e-folding scale of 20 m (Paulson and Simpson 1977).

While CASE satisfies Eq. (7) in each 3-month assimilation window, there are discontinuities in the heat budget at the transition of the windows. The optimized solution of every 3-month window is a forward integration of the model forced with adjusted controls so that Eq. (7) is exact during those 3 months. However, the final state of a 3-month solution is generally warmer than the starting state of the subsequent 3 months, which is initialized from HYCOM global 1/12° daily analysis and then optimized. The difference in potential temperature at the boundary between 3-month intervals is referred to as an increment. A preliminary assessment of the increment spatial structure (not shown) revealed that increments were largest at the surface, near the coast, and during the summer, suggesting that the excess heat input was from air–sea heat flux of the atmospheric forcing. Assimilation increments for temperature have been previously diagnosed and used to calculate uncertainties and adjustments in global state estimates (Carton et al. 2018; Valdivieso et al. 2017). Here, the temperature increment (°C) is calculated at every grid point and transition time, then converted to a rate of change of temperature (°C s^{-1}) and distributed uniformly over the 3-month assimilation window. This allows treating it as a uniform adjustment in the budget that can be combined with the temperature tendency term instead of a delta function forcing every 3 months. We convert it to a heat flux and refer to it in the budget as the heat adjustment, denoted Q_{adj} with units of watts per meter cubed. We add Q_{adj} to the tendency term to calculate an adjusted tendency term:

$$\frac{\partial T_{\text{adj}}}{\partial t} = \frac{\partial T}{\partial t} + \frac{Q_{\text{adj}}}{\rho_o c_p}. \tag{8}$$

For almost all 3-month windows, Q_{adj} is negative and thus the adjusted tendency is less than the model tendency. The heat adjustment acts to correct the warm bias. Applying the heat adjustment to Eq. (7) yields

$$\underbrace{\rho_o c_p \frac{\partial T_{\text{adj}}}{\partial t}}_{\text{adjusted temperature tendency}} = \underbrace{\frac{\partial Q}{\partial z}}_{\text{air−sea heat flux}} - \rho_o c_p \left[\underbrace{\mathbf{u} \cdot \nabla T}_{\text{heat advection}} - \left(\underbrace{\kappa_H \nabla_H^2 T + \kappa_Z \frac{\partial^2 T}{\partial z^2} + K_T^{\text{turb}}}_{\text{heat diffusion}} \right) \right] + \underbrace{Q_{\text{adj}}}_{\text{heat adjustment}}, \tag{9}$$

where the adjustment appears on both sides of the equation (implicitly in the adjusted temperature tendency term on the left and explicitly on the right) to maintain budget closure.

Beyond the gridpoint heat balances, we are interested in heat balances within various volumes, including NBox and SBox volumes (Fig. 2). Applying a volume integral to Eq. (9) yields

$$\underbrace{\rho_0 c_p \iiint_V \frac{\partial T_{\text{adj}}}{\partial t} dV}_{\text{TTEND}} = \underbrace{\int_A \left(Q_{z_2} - Q_{z_1} \right) dx\, dy}_{\text{TFLUX}} - \underbrace{\rho_0 c_p \iiint_V (\mathbf{u} \cdot \nabla T)\, dV}_{\text{ADV}} + \underbrace{\rho_0 c_p \iiint_V \left(\kappa_H \nabla_H^2 T + \kappa_Z \frac{\partial^2 T}{\partial z^2} + K_T^{\text{turb}} \right) dV}_{\text{DIF}}$$

$$+ \underbrace{\iiint_V Q_{\text{adj}}\, dV}_{\text{ADJ}}, \tag{10}$$

which has units of watts but becomes watts per meter squared when divided by the area. The volume-integrated heat budget terms in Eq. (10) are adjusted temperature tendency (TTEND), air–sea heat flux (TFLUX), heat advection (ADV), heat diffusion (DIF), and heat adjustment (ADJ).

3. Results

a. Volume budgets

1) MEAN

The mean three-dimensional circulation of the upper 50 m is composed of horizontal geostrophic and ageostrophic flow, and coastal upwelling (Fig. 1). The geostrophic velocity field includes a poleward California Undercurrent nearshore and a meandering equatorward California Current offshore (Fig. 1a), circulation features that are also apparent in the −500–0-m-depth average (Zaba et al. 2018). The ageostrophic velocity field is predominantly wind-driven surface Ekman flow (Fig. 1b) moving offshore, perpendicular to the driving equatorward alongshore winds (Chereskin 1995). Upwelling is apparent as a band of positive vertical velocity between the coast and

approximately 175–400 km offshore (Fig. 1c). By volume conservation, divergent Ekman transport at the coastline (Fig. 1b) drives strong upwelling, as seen in the band of dark red along the coast (Fig. 1c). The thin band of strong vertical velocity is roughly 30–40 km wide in the CASE mean. Positive wind stress curl drives slower, broader upwelling offshore (Fig. 1c). Figure 1 depicts the classic upwelling overturning cell: water is vertically transported upward at the coast to replace the surface water that has been transported offshore by alongshore winds (Davis 2010; Nelson 1977).

Calculated over the upper 50 m, the time-mean volume budgets of NBox and SBox quantify the transports associated with that upwelling overturning cell (Fig. 2), which include upward vertical transport through the bottom wall and offshore transport across the west wall. The results shown in Fig. 2 are the solutions to Eq. (4), where $z_1 = -50$ m. The cross-shore transport out of SBox (−0.08 Sv) is less than that of NBox (−0.13 Sv) as a result of greater onshore geostrophic transport opposing the offshore Ekman transport across the west wall of SBox than NBox (Figs. 3c,d). Both boxes span the width of the poleward California Undercurrent, which exhibits flow continuity from south of line 90 to north of line 66.7
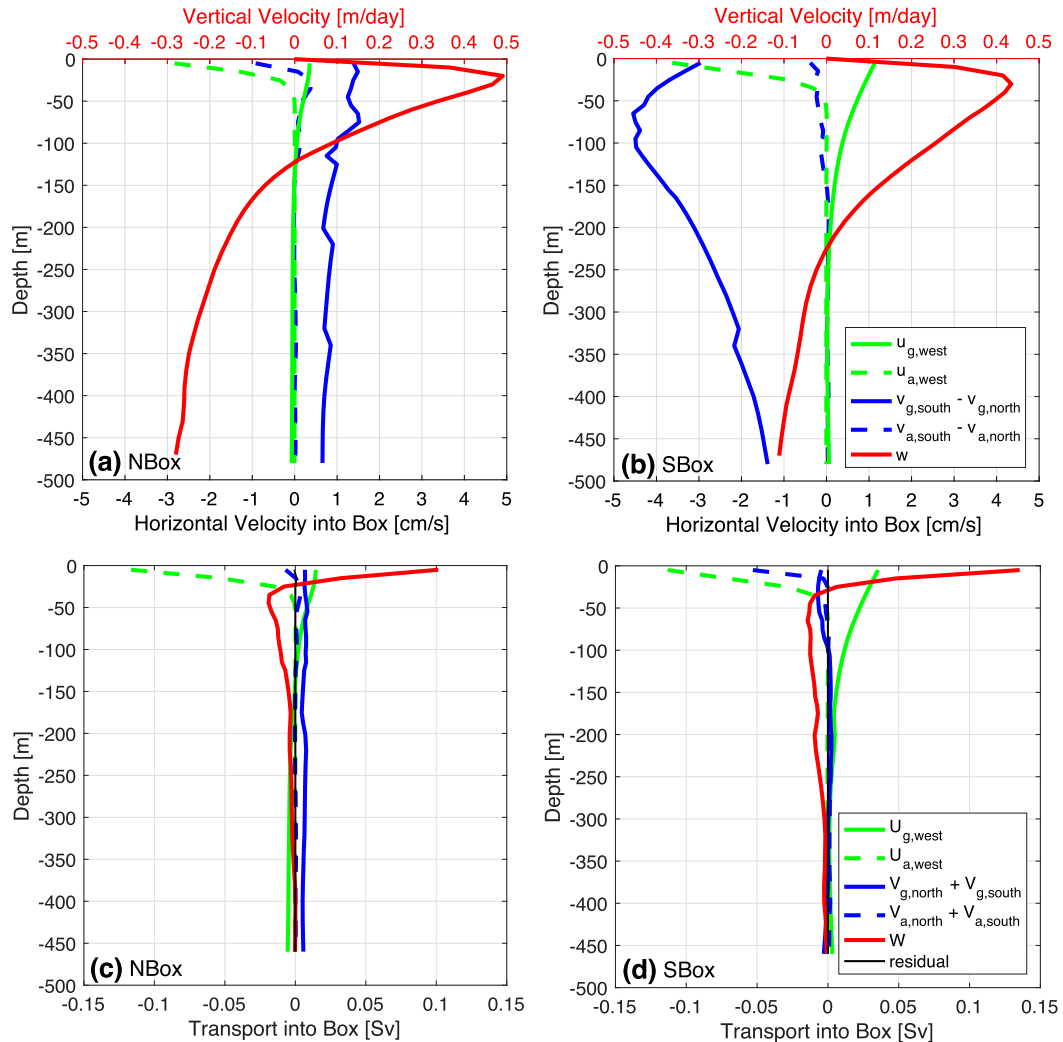
FIG. 3. Depth profiles of 2007–13 mean (a),(b) velocity components and (c),(d) volume transports per model depth cell into (left) NBox and (right) SBox. Cross-shore velocity (green) and alongshore velocity convergence (blue) are decomposed into geostrophic (solid line) and ageostrophic (dashed line) components, perimeter averaged at each discrete depth cell over the box wall normal to the flow, and are plotted relative to the bottom x axis of (a) and (b) in units of centimeters per second. Vertical velocity (red) is area averaged over the horizontal surface area enclosed by the box perimeter and is plotted relative to the top x axis of (a) and (b) in units of meters per day. The volume budget terms in (c) and (d) are defined as in Eq. (6) and are calculated over each model cell with bottom boundary z_1, top boundary z_2, and height $z_2 - z_1$, which is 10–20 m depending on depth in the water column. The residual term in (c) and (d) is the sum of all terms in Eq. (6); it is zero where volume is conserved.

(Fig. 1a and Fig. 2), with mean alongshore divergence in SBox and convergence in NBox.

Time-mean velocities are depth varying, as shown in Figs. 3a and 3b. At each depth level, the horizontal velocities (u and v) are perimeter averaged over the box wall through which they flow perpendicular (i.e., u is perimeter averaged over the west wall, and v is perimeter averaged over the south and north walls). Vertical velocity w is area averaged at each depth level. For both boxes, the offshore Ekman velocity profile across the west wall is strongest at the surface and decays to zero by

roughly −45-m depth. The maximum Ekman velocity at the surface is about $3\,\mathrm{cm\,s^{-1}}$. Of smaller magnitude by a factor of 1/6–1/3, an opposing onshore geostrophic velocity flows into the boxes, although it is about 2 times as strong and extends 2 times as deep in SBox (Fig. 3b) as in NBox (Fig. 3a). There is an alongshore geostrophic velocity divergence in SBox (Fig. 3b), meaning the poleward velocity is greater across Line 80 than Line 90, and weak alongshore geostrophic convergence in NBox (Fig. 3a), meaning the poleward velocity is greater across Line 80 than Line 66.7. Alongshore ageostrophic convergence is relatively
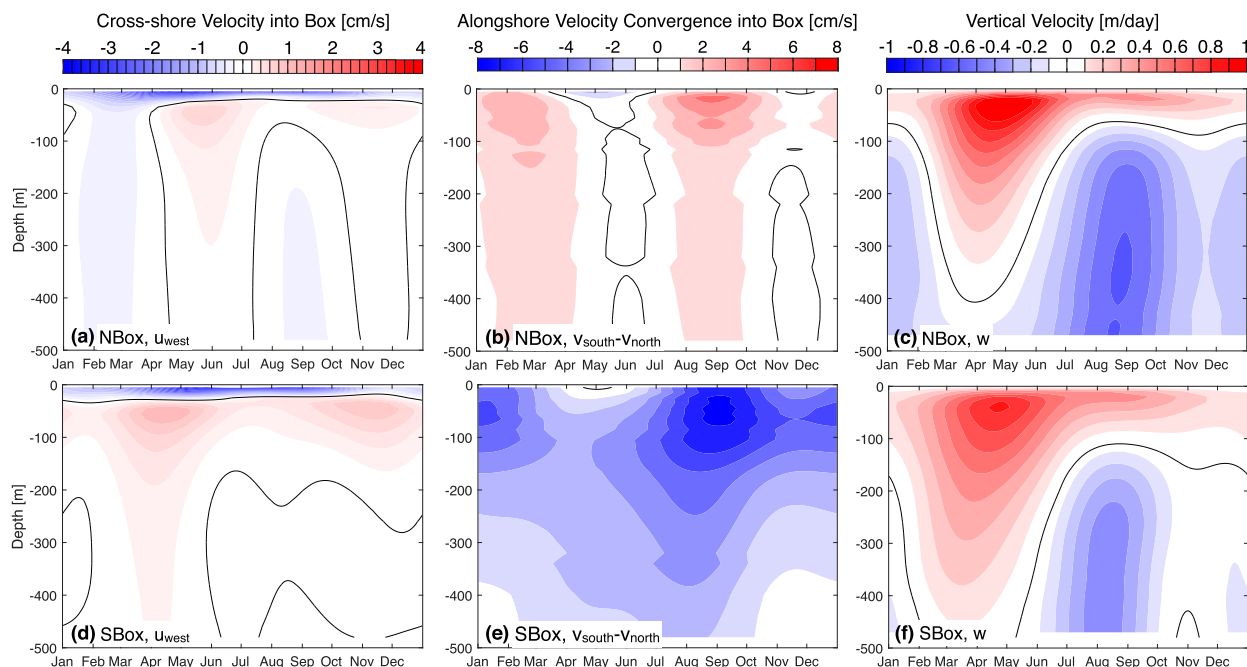
FIG. 4. Annual cycles of the velocity components into (top) NBox and (bottom) SBox plotted as a function of time and depth. As in Fig. 3, (a),(d) cross-shore velocity and (b),(e) alongshore velocity convergence are perimeter averaged and (c),(f) vertical velocity is area averaged. The horizontal velocity fields in (a), (b), (d), and (e) are displayed in units of centimeters per second, where red indicates one-dimensional flow convergence within the box perimeter and blue indicates divergence. Vertical velocities in (c) and (f) are displayed in units of meters per day, where red is upward and blue is downward. The black line is the zero-velocity contour.

insignificant. In both boxes, the vertical velocity profile is positive (upwelling) near the surface and negative (down-welling) at depth (Figs. 3a,b). However, that zero-crossing is about 100 m deeper in SBox (~ -225 m) than in NBox (~ -125 m), suggesting that the upwelling overturning cell may be deeper in the SCB. Maximum vertical velocities of 0.43–0.49 m day^{-1} peak at roughly -25-m depth.

Volume budgets are calculated discretely within each model cell, the thickness of which telescopes from 20 m at -500-m depth to 10 m at the surface, and the vertical profiles of the budget terms, defined as in Eq. (6), are shown in Figs. 3c and 3d. The terms are largest in the upper 30 m, where the dominant balance is between vertical transport convergence and off-shore Ekman transport divergence. Below -30-m depth, the vertical transport in each depth cell is divergent be-cause the upward velocity is greater across the top boundary of the grid cell than the bottom boundary (Figs. 3a,b). The vertical divergence below -30 m is bal-anced by alongshore geostrophic transport convergence in NBox (Fig. 3c) and onshore geostrophic transport in SBox (Fig. 3d).

2) ANNUAL CYCLE

The seasonal cycle of coastal circulation is charac-terized by semiannual strengthening of the alongshore

CU in summer and winter (Gomez-Valdivia et al. 2017; Rudnick et al. 2017a; Zaba et al. 2018), and an annual maximum in wind-driven upwelling and offshore Ekman transport from spring to early summer. At the times of CU strengthening, there is a convergence of alongshore velocity in NBox (Fig. 4b) and an alongshore divergence in SBox (Fig. 4e). The depth of maximum convergence/divergence is subsurface (from -55 to -20 m) collocated with the CU core depth. In both boxes, the wind-driven Ekman velocity flows offshore in a thin layer 20–30 m thick year round (Figs. 4a,d), though it is strongest in late spring and summer. An onshore flow of weaker magnitude exists below the Ekman flow and ex-hibits a weak semiannual cycle, strengthening in April/May and November when the magnitude of alongshore di-vergence is weakest (Figs. 4b,e). Throughout the entire year, there is a subsurface vertical velocity divergence, with upward velocity near the surface and downward velocity below (Figs. 4c,f). However, the strength of the vertical velocities and the depth of the zero-crossing ex-hibit substantial seasonal variability. During the spring, almost the entire vertical velocity profile is positive (up-ward). The maximum of the springtime vertical velocity profile is roughly at -50 m, which also happens to be the mean depth of the top of the thermocline. Throughout the remainder of the year, a larger fraction of the upper
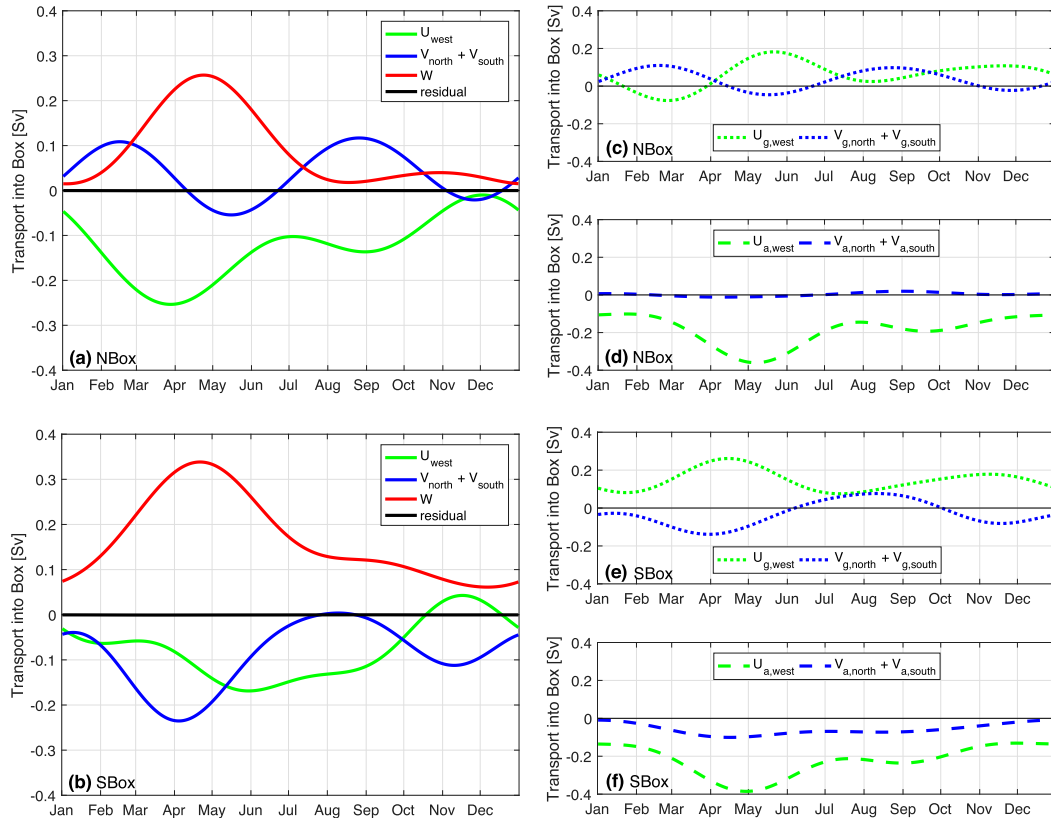
FIG. 5. Annual cycle of −50–0-m volume budgets of (a) NBox and (b) SBox. The cross-shore (green), alongshore (blue), and vertical (red) transports are defined and computed as in Eq. (4), with $z_1 = -50$ m where positive transport is into the box. The residual term in (a) and (b) is the sum of all terms in Eq. (4); it is zero everywhere, indicating volume conservation. Also shown is the decomposition of horizontal transport into (c),(d) NBox and (e),(f) SBox, where (c) and (e) show the geostrophic transport (dotted lines) and (d) and (f) show the ageostrophic transport (dashed lines).

500 m of the water column is downwelling. Figures 4c and 4f indicate that the depth of the overturning cell and source waters for upwelling vary over the course of the year. They also vary spatially, for example the depth of positive vertical velocity extends about 100 m deeper in SBox than in NBox. Previous overturning cell depth estimates range from −300 to −50 m (Talley et al. 2011), all of which may be correct depending on the time of year and location being examined.

Area-integrated transports into the upper 50 m of NBox and SBox are shown in Fig. 5. Vertical transport into the box is always positive with a maximum in April during peak upwelling season (Figs. 5a,b). Cross-shore transport is offshore across the west wall. The alongshore convergence/divergence has a semiannual cycle that compensates the convergence/divergence of the cross-shore upwelling cell. A decomposition of the horizontal volume transport confirms that the cross-shore ageostrophic component is out of the box (offshore) (Figs. 5d,f). This is the wind-driven surface Ekman transport. In contrast, the cross-shore geostrophic

component over the same depth range is onshore from April to mid-January in NBox (Fig. 5c) and all months of the year in SBox (Fig. 5e). The alongshore flow convergence is predominately geostrophic (Figs. 5c–f).

3) 2014–16 ANOMALIES

An analysis of the interannual volume budget relative to the annual cycle (Fig. 5) indicates that all components of the 3D circulation were anomalous, though at different times. Over the years 2013.5–16.5, there was a downwelling anomaly across −50-m depth for 597 of the 1096 days (~54%) within NBox (Fig. 6a) and 625 of the 1096 days (~57%) within SBox (Fig. 6b). These downwelling anomalies are primarily due to reduced upward transport, except for two time periods in NBox (15 November 2013–6 January 2014 and 9 August 2014– 9 January 2015) when downward transport across −50-m depth occurred (Fig. 6a). Both reduce the vertical transport of cold, saline water toward the ocean surface. Over 2013.5–16.5, the downwelling transport anomaly is balanced most often by alongshore convergence
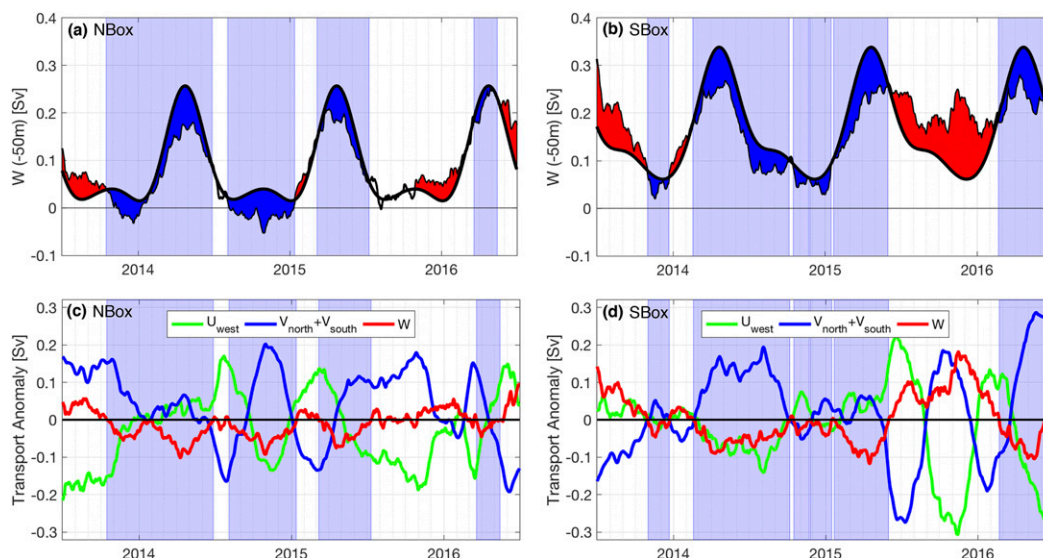
FIG. 6. Time series over years 2013.5–16.5 of (a),(b) vertical transport across −50-m depth and (c),(d) all −50-0-m volume budget term anomalies of (left) NBox and (right) SBox. In (a) and (b), the thick solid black line is the repeated annual cycle as in Figs. 5a and 5b, the thin black line is the interannual signal smoothed with a 3-month running mean, the opaque color fill denotes positive (red) and negative (blue) interannual anomalies of 30+-day duration, and the background blue color bands highlight just those time periods of negative vertical transport anomaly. Positive transports and transport anomalies are defined as into the box. In (c) and (d), the cross-shore (green), alongshore (blue), and vertical (red) transport anomalies sum to zero.

anomalies and sometimes by onshore transport anomalies (Figs. 6c,d). The timeline of 3D circulation anomalies in the upper 50 m is complex and a detailed explanation of every instantaneous volume balance shown in Figs. 6c and 6d is neither feasible nor necessary. Instead, we explain the volume budget anomalies during each box's longest sustained downwelling anomaly period. During October 2013–June 2014, the downwelling anomaly in NBox (Fig. 6a) is balanced initially by alongshore transport convergence (October–January), then by a combination of alongshore transport convergence and onshore transport anomaly (January–May), and finally just by an onshore transport anomaly (May–June) (Fig. 6c). Onshore transport anomalies could be due to a weakening of the cross-shore upwelling overturning cell and/or the onshore displacement of the offshore California Current during 2014 that was observed by Zaba and Rudnick (2016). For the duration of February–October 2014, the downwelling anomaly in SBox (Fig. 6b) is balanced by alongshore transport convergence, which also balances the concurrent offshore anomaly of cross-shore transport (Fig. 6d). Another interesting, and somewhat unexpected, signal is the strong upwelling anomaly into SBox over June 2015–February 2016 (Fig. 6b), which was balanced by an alongshore divergence anomaly (June–August), an offshore transport anomaly (September–December), and another alongshore divergence anomaly (December–

February) (Fig. 6d). Strong upwelling-favorable winds occurred during that time period (Frischknecht et al. 2017; Jacox et al. 2016).

b. Heat budgets

1) MEAN

The dominant terms of the time-mean mixed layer (from −50 to 0 m) heat budget are air–sea heat flux and heat advection, followed closely by the heat adjustment term (Fig. 7). In both boxes, air–sea heat flux is positive (i.e., downward into the ocean), largest at the surface and decaying exponentially with depth to values $< 1\,\text{W m}^{-2}$ by −75-m depth (Figs. 7a,b). Heat advection is negative (i.e., cooling) in the upper 80–85 m and slightly positive (i.e., warming) below that depth ($\sim 1\,\text{W m}^{-2}$) (Figs. 7a,b). Diffusion has a cooling effect from −10 to 0 m in NBox and from −20 to 0 m in SBox and a warming effect of smaller magnitude below (Figs. 7a,b). Vertical diffusion and mixing act on a positive vertical temperature gradient, thereby cooling the surface layer and warming the layer underneath. The heat adjustment term ranges from −10 to $-7\,\text{W m}^{-2}$ at the surface (Figs. 7a,b), of similar magnitude to near-surface heat diffusion and heat advection. It has a similar shape and vertical decay rate as the air–sea heat flux term but opposite sign, supporting the notion that the excess heat in CASE is due to excess heating by the atmosphere at the air–sea interface.
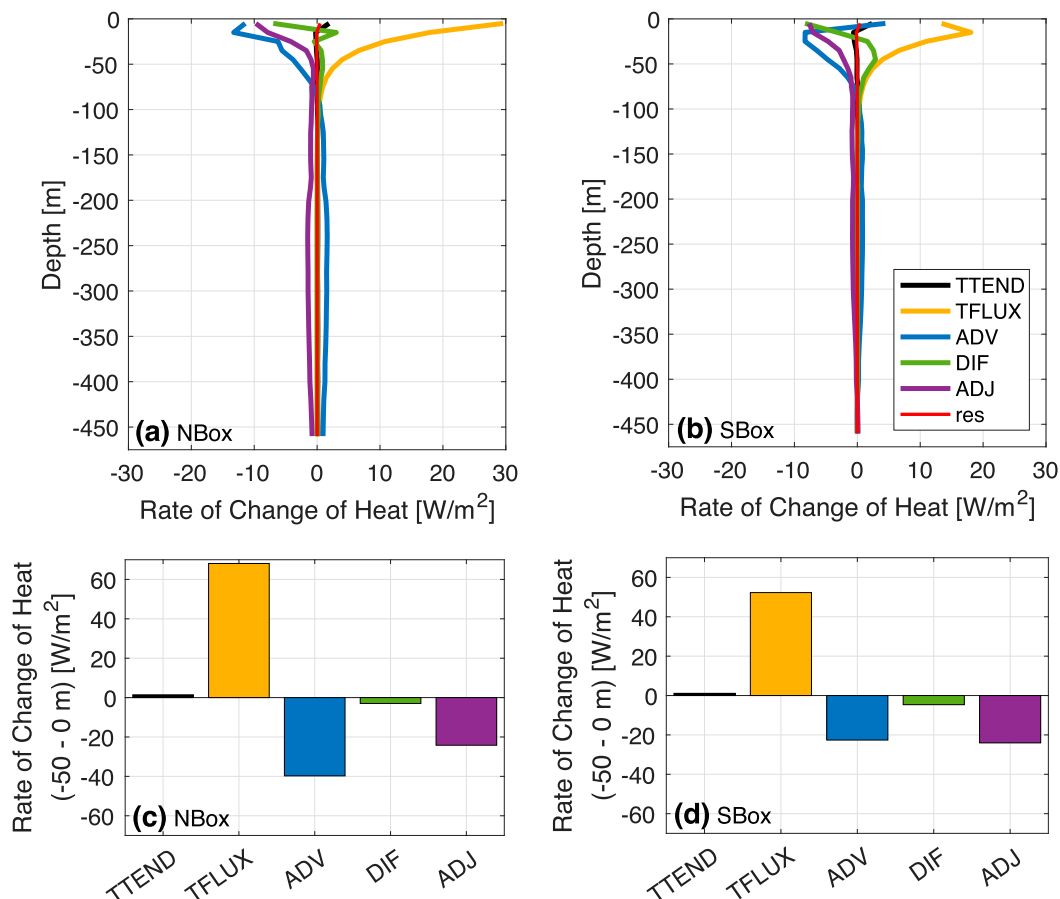
FIG. 7. (a),(b) Depth-dependent and (c),(d) −50–0-m depth-integrated 2007–13 mean heat budget terms area averaged over (left) NBox and (right) SBox. In units of watts per meter squared, the terms are adjusted temperature tendency (TTEND; black), air–sea heat flux (TFLUX; gold), total heat advection (ADV; blue), total heat diffusion (DIF; green), and heat adjustment (ADJ; purple), defined as in Eq. (10). Terms are calculated over the height of each depth cell ($z_2 - z_1$, where z_1 and z_2 are the cells' bottom and top boundaries) in (a) and (b) and over the upper 50 m (where $z_1 = -50$ m and $z_2 = 0$ m) in (c) and (d). The residual term (red) in (a) and (b) is the difference between TTEND and the sum of all of the other terms (TFLUX + ADV + DIF + ADJ); it is zero where heat is conserved.

Integrated from −50 to 0 m (Figs. 7c,d), mean air–sea heat flux warms the volumes at a rate of 68 (NBox) and 52 (SBox) W m^{-2}, mean heat advection cools them at a rate of −40 (NBox) and −23 (SBox) W m^{-2}, and mean heat diffusion cools at a much lower rate of −3 (NBox) and −5 (SBox) W m^{-2}. The heat adjustment term is about −24 W m^{-2} in both boxes (Figs. 7c,d). The nonzero adjusted tendency term is slightly positive (1–1.5 W m^{-2}) either indicating the remnants of a warm bias after the adjustment or a small secular warming trend over 2007–13 (Figs. 7c,d). These heat budgets calculated over NBox and SBox close to within 0.02%.

2) ANNUAL CYCLE

Heat content of the upper 50 m of NBox and SBox increases from May to mid-October and decreases over the remainder of the year (Figs. 8a,b). Potential temperature tendency is generally in phase with air–sea heat flux, both terms peak in June. Heat advection is nearly 180° out of phase with potential temperature tendency and air–sea heat flux, acting to cool the water from March to September (SBox) or October (NBox) and doing so most effectively in April–May during peak upwelling season. During late autumn and winter, heat advection into the boxes is positive (i.e., warming). Vertically integrated from −50 to 0 m, heat diffusion is negative throughout the year (Figs. 8c,e), acting to cool the upper 50 m, although its contribution to the volume-integrated heat budget is an order of magnitude smaller than that of the other terms (Figs. 8a,b). However, the depth-dependent diffusion is a significant term within shallower depth cells (Figs. 8d,f). Calculated over 10-m
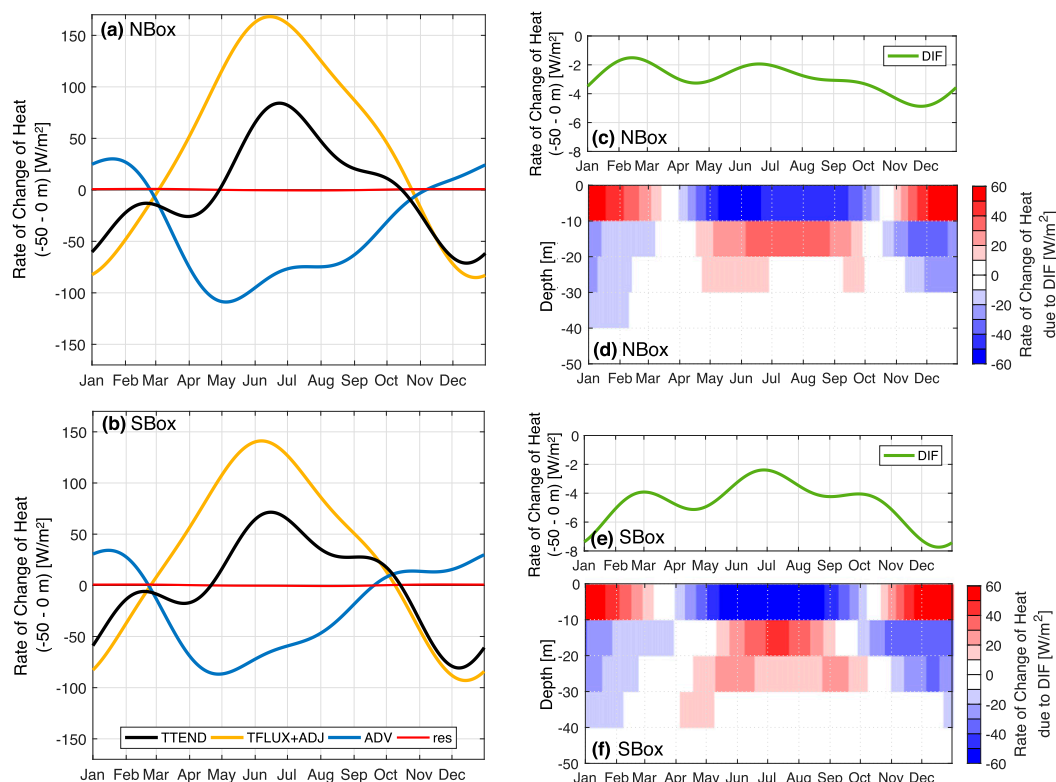
FIG. 8. (a)–(c),(e) Depth-integrated and (d),(f) depth-dependent annual cycles of heat budget terms area averaged over NBox in (a), (c), and (d) and SBox in (b), (e), and (f). The adjusted temperature tendency (TTEND; black), adjusted air–sea heat flux (TFLUX + ADJ; gold), total heat advection (ADV; blue), and total heat diffusion (DIF; green) terms in (a)–(c) and (e) are defined as in Eq. (10), with $z_1 = -50$ m and $z_2 = 0$ m. The residual term (red) is the difference between TTEND and the sum of all other terms (TFLUX + ADV + DIF + ADJ); it is zero where heat is conserved. DIF in (d) and (f) is calculated over the height of each depth cell ($z_2 - z_1$, where z_1 and z_2 are the cells' bottom and top boundaries).

depth cells centered on -5, -15, and -25 m, the rate of change of heat due to diffusion has an apparent annual cycle with an amplitude of several tens of watts per meter squared. The annual cycle of heat diffusion is depth dependent: there is a 180° phase shift between the depth cells centered on -5 and -15 m, and the amplitude decreases with depth. In the summer, heat diffusion is minimum within the depth cell centered on -5 m and maximum within the depth cell centered on -15 m, peaking in July (Figs. 8d,f). Summer is also the time of maximum downward air–sea heat flux (Figs. 8a,c). Therefore, vertical diffusion mixes the heat downward, cooling the shallowest layer and warming the layer below it. The opposite is true during the winter months when air–sea heat flux is negative (Figs. 8a,b): heat diffusion is maximum within the depth cell centered on -5 m and minimum within the depth cell centered on -15 m. The diffusion term acts to redistribute heat between adjacent depth cells; however, its effects are strongly surface intensified and its net contribution to the integrated mixed layer heat budget is insignificant.

3) 2014–16 ANOMALIES

In the 10-yr CASE model solution, the warmest CCS mixed layer temperatures occur during 2014–16 (Zaba et al. 2018). Prior to the calculation of heat budgets over fixed coastal volumes, we examine the air–sea heat flux anomalies over the larger model domain. Net downward air–sea heat flux Q_0, spatially averaged over the oceanic (i.e., land free) model domain of Fig. 1, is shown in Fig. 9. Daily Q_0 values fluctuate vastly around the annual cycle (Fig. 9a); however, over 2013.5–16.5 there are three 1-month periods of sustained (30+ day) Q_0 anomalies: January 2014 (positive), May 2015 (negative), and February 2016 (positive). The anomaly extremes during those time periods are $+85$ and -141 W m^{-2}. Both the magnitude and the duration of these anomalies are relevant to the mixed layer heat budget. Smoothing Q_0 with a 3-month running average (Fig. 9b) reveals the Q_0 anomaly patterns at seasonal scales. Over the 3-yr period shown, the months in late autumn, winter, and early spring tend to have positive Q_0 anomalies, whereas the summer months have negative Q_0
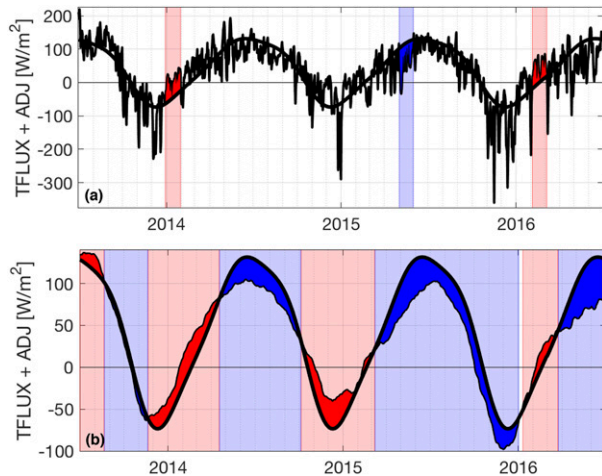
FIG. 9. Time series over 2013.5–16.5 of net surface heat flux Q_0 spatially averaged over the land free domain of Fig. 1 (128°–116°W, 30°–38°N). Positive is defined as downward into the ocean. The thick solid black line is the repeated annual cycle, and the thin black line is the interannual signal (a) unfiltered and (b) filtered with a 3-month running mean [note the different y axis limits of (a) and (b)]. The opaque color fill and the background color bands denote positive (red) and negative (blue) interannual anomalies of 30+-day duration.

anomalies. At the spatial scale of the model domain, air–sea heat flux anomalies at daily (Fig. 9a) and monthly (Fig. 9b) time scales are variable over the 2014–16 period. Also, Q_0 played a role in the initial forcing of the 2014–16 mixed layer heat anomaly but it did not maintain the anomaly during its entirety.

Anomalously warm temperatures are apparent during the entirety of 2014–16.5 (Figs. 10a,b), with volume-averaged −50–0-m adjusted potential temperature T_{adj} peaking in October 2014 and 2015. In October 2014, T_{adj} reaches 16.9°C in NBox and 18°C in SBox, both ~2°C above their respective annual cycles. The following year, October 2015 anomalies exceed the annual cycle by ~3°C with T_{adj} values reaching 17.5°C (NBox) and 19°C in (SBox). Over 2013.5–16.5, temperature tendency is above average for several time periods of 1.5–6.2-month duration (Figs. 10c,d), including the 2–4 months preceding the aforementioned T_{adj} October maxima. The temperature tendency shown in Figs. 10c and 10d is filtered with a 3-month running mean to extract anomalies at seasonal scales; the unfiltered daily temperature tendency (not shown) is much more variable, with positive anomalies lasting only 3 weeks or less. Here we construct a timeline of the dominant heat budget term [Eq. (10)] anomalies that contribute to the anomalous rates of change of heat. In NBox, excess temperature tendency is driven by positive anomalies in air–sea heat flux during September–October 2013, February–May

2014, December 2014–January 2015, and August–September 2015, heat advection during August–November 2014, and equal contributions from both mechanisms during November 2013–January 2014 (Fig. 10e). The anomalous heat advection components in NBox are: alongshore (November 2013–January 2014 and August–November 2014) and vertical (August–November 2014) (Fig. 10g). In SBox, the driving anomalies are air–sea heat flux during November 2014–January 2015, heat advection during July–October 2013 and July–September 2014, and both during November–December 2013, October–November 2014, and July–September 2015 (Fig. 10f). The anomalous heat advection components in SBox are alongshore (July 2013–January 2014 and July–September 2015) and vertical (July–September 2014) (Fig. 10h). There is a notable positive cross-shore heat advection anomaly in SBox from late 2014 to mid-2015; however, it is balanced by a negative alongshore heat advection anomaly. The T_{adj} time series extreme in October 2015 is driven by air–sea heat flux in NBox and by air–sea heat flux and alongshore heat advection in SBox. These results emphasize that the heating mechanisms contributing to the warming vary over 2013.5–16.5 and between regions.

The −50–0-m volume-integrated heat diffusion anomalies are on the order of 1 W m^{-2} (Figs. 11a,b), an order of magnitude smaller than the temperature tendency, air–sea heat flux, and heat advection anomalies (Figs. 10e–h). The largest interannual heat diffusion excursions occur in November 2015–January 2016, when the negative anomalies reach ~−3.5 (NBox; Fig. 11a) and ~−8 (SBox; Fig. 11b) W m^{-2}. Winter 2015/16 saw strong equatorward winds (Frischknecht et al. 2017; Jacox et al. 2016), which acted to mix the upper ocean, warming the surface layer (from −10 to 0 m) but cooling the layers below (Fig. 11d). The net effect is cooling over the mixed layer.

Interannual warm anomalies were not limited to the upper 50 m of the water column. Glider observations and CASE both capture a positive subsurface 26.0 kg m^{-3} isopycnal salinity anomaly at CalCOFI line 90 (Zaba et al. 2018), which has a mean depth of roughly −100 m near the coast. By compensation, the positive salinity anomaly is accompanied by a positive potential temperature anomaly, which peaks at the same time as the equatorial El Niño at the turn of the year 2015/16 (Fig. 12b). The strongest 26.0 kg m^{-3} isopycnal warming occurs along the coast and south of Point Conception, in the SCB and off the coast of northern Baja California. The spatial structure of the 26.0 kg m^{-3} isopycnal temperature anomaly in Fig. 12b suggests the tropical influence of heat advection by the narrow, nearshore CU. Anomalous poleward heat advection was also observed during the strong 1997/98 El Niño event (Lynn and Bograd 2002).
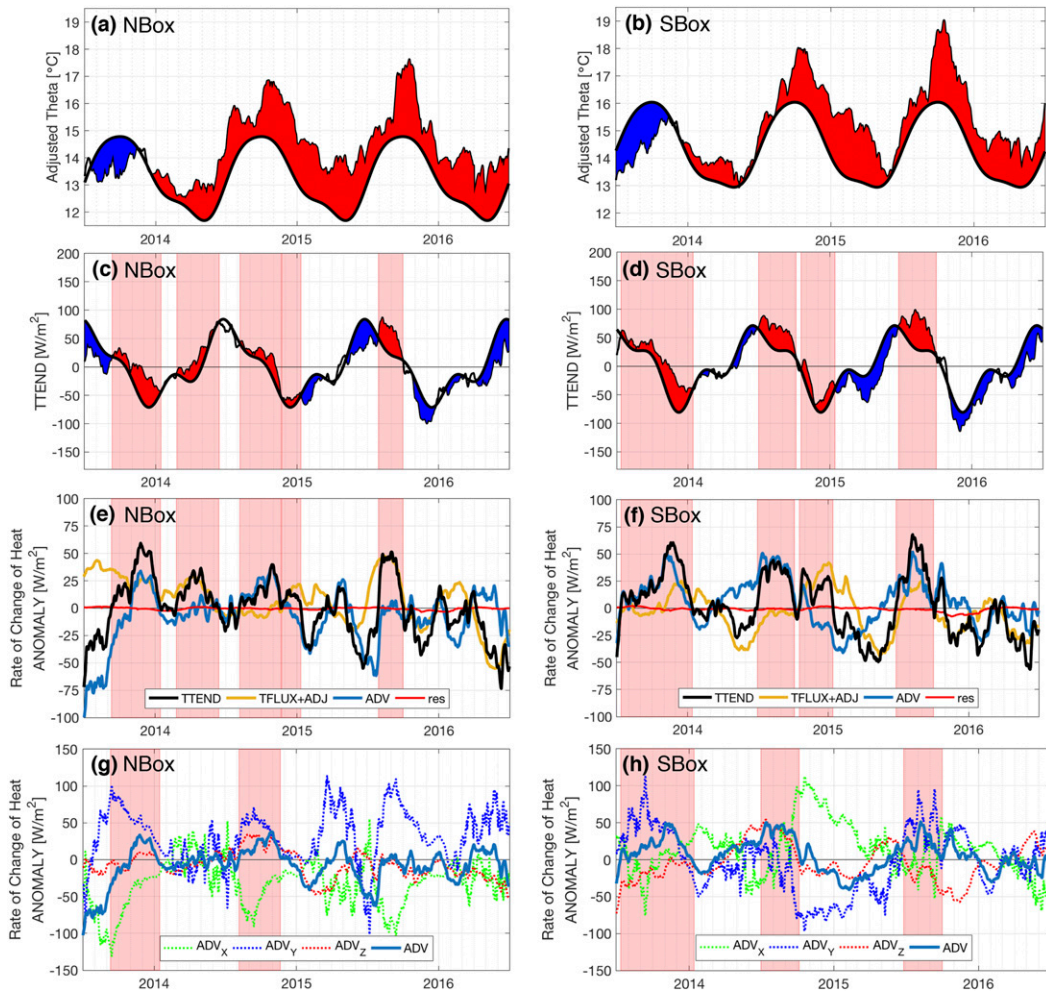
FIG. 10. Time series over 2013.5–16.5 of (a),(b) volume-averaged adjusted potential temperature; also shown are times series of volume-integrated and area-averaged (c),(d) adjusted temperature tendency and (e)–(h) heat budget term anomalies. The volume is bound laterally by (left) NBox and (right) SBox and vertically by depths of -50 and 0 m. In (a)–(d), the thick solid black line is the repeated annual cycle, the thin black line is the interannual signal [unfiltered in (a) and (b); filtered with a 3-month running mean in (c) and (d)], and the opaque color fill denotes positive (red) and negative (blue) interannual anomalies of 30+-day duration. The background red color bands highlight the time periods of positive temperature tendency anomaly due to any mechanism in (c)–(f) and due to positive heat advection anomaly in (g) and (h). In (e) and (f), the heat budget terms are defined as in Eq. (10): adjusted temperature tendency (TTEND; black), adjusted air–sea heat flux (TFLUX + ADJ; gold), and total heat advection (ADV; blue). The residual term (red) in (e) and (f) is the difference between TTEND and the sum of TFLUX + ADV + ADJ; it is zero when heat is conserved. In (g) and (h), total heat advection is further decomposed into cross-shore (ADV$_X$; dotted green), along-shore (ADV$_Y$; dotted blue), and vertical (ADV$_Z$; dotted red) components.

No coherent $26.0 \, \text{kg m}^{-3}$ isopycnal temperature anomaly is present during the MHW of the previous winter (Fig. 12a).

The absolute maximum of $-(210–100)$-m volume-integrated T_{adj} in SBox is $\sim 10.7°$C ($+1.3°$C anomaly) on 10 December 2015 (Fig. 13a). Preceding the T_{adj} maximum, a pronounced rise in T_{adj} begins around 1 September 2015 (Fig. 13a) along with a positive heat advection anomaly (Fig. 13b). The date 1 September is roughly when the heat advection annual cycle maximum occurs; however, in 2015, heat advection continued to

increase into the autumn rather than decrease (Fig. 13b). A decomposition of heat advection into directional components (Fig. 13c) reveals that horizontal (not vertical) heat advection anomalies were positive in autumn 2015; lateral advection is the forcing mechanisms of the subsurface warming.

A further decomposition of lateral heat advection (Fig. 14) reveals both CU poleward volume transport and CU temperature to be driving the anomalous subsurface heat content. In September 2015, anomalous
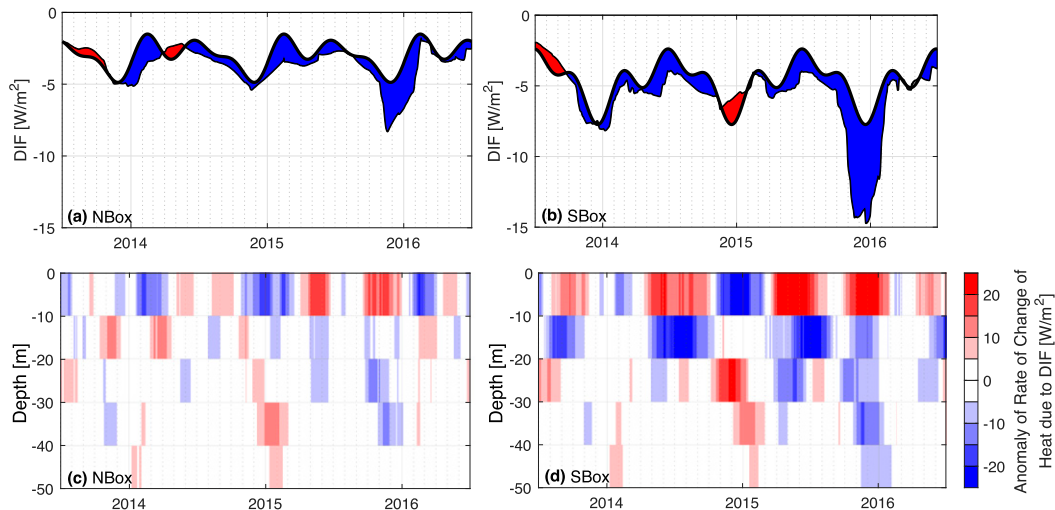
FIG. 11. Time series over 2013.5–16.5 of (a),(b) depth-integrated and (c),(d) depth-dependent heat diffusion (DIF) area averaged over (left) NBox and (right) SBox. DIF is defined as in Eq. (10) and is calculated over the upper 50 m ($z_1 = -50$ m and $z_2 = 0$ m) in (a) and (b) and over the height of each depth cell ($z_2 - z_1$, where z_1 and z_2 are the cells' bottom and top boundaries) in (c) and (d). In (a) and (b), the thick solid black line is the repeated annual cycle, the thin black line is the interannual cycle filtered with a 3-month running mean, and the opaque color fill denotes positive (red) and negative (blue) interannual anomalies of 30+-day duration. Anomalies from the annual cycle are shown in (c) and (d).

heat transport comes into SBox across its south wall (Fig. 14a). Northward volume transport across the SBox south wall is also anomalously positive at that time (Fig. 14b), specifically over 27 August–21 September 2015. On 12 September 2015, the largest volume transport (~2.1 Sv) and anomaly (~+1.4 Sv) of the 2013.5–16.5 period occur. The volume transport anomaly could be caused by CU strengthening or broadening or both. In addition, temperature values perimeter averaged over the south wall and vertically

averaged from -210 to -100 m were anomalously positive by over 1°C during September–December 2015 (Fig. 14c), meaning the CU transported anomalously warm water from the south. A quick rise in south wall temperature occurs at the same time as the volume transport anomaly across south wall, suggesting that a sharp temperature gradient moved into the SCB. There are no equivalently pronounced positive heat transport anomalies across the SBox west nor north walls (Fig. 14a).
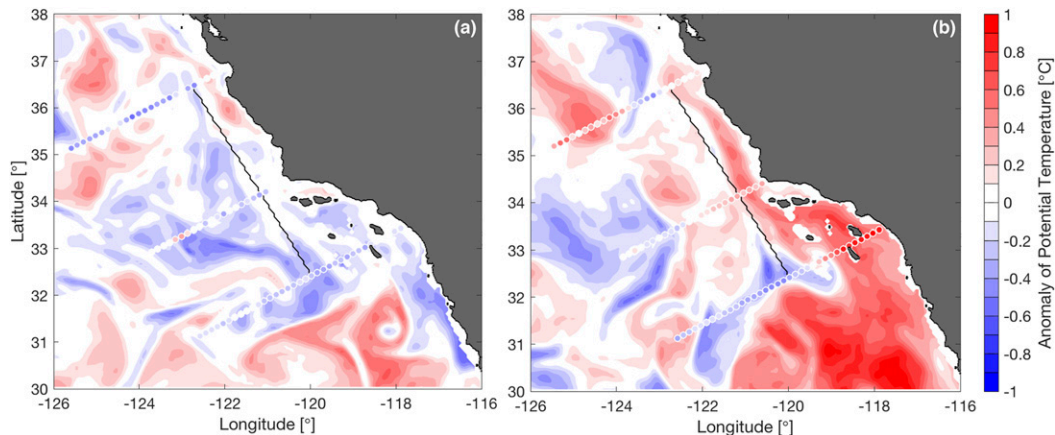

FIG. 12. Potential temperature anomaly on the 26.0 kg m^{-3} isopycnal surface temporally averaged over (a) December 2014–January 2015 and (b) December 2015–January 2016. Filled color contours represent CASE model output, and color-filled dots represent CUGN mapped measurements (subsampled at 15 km), both with the same color bar. The thin black line is the western boundary of NBox and SBox.
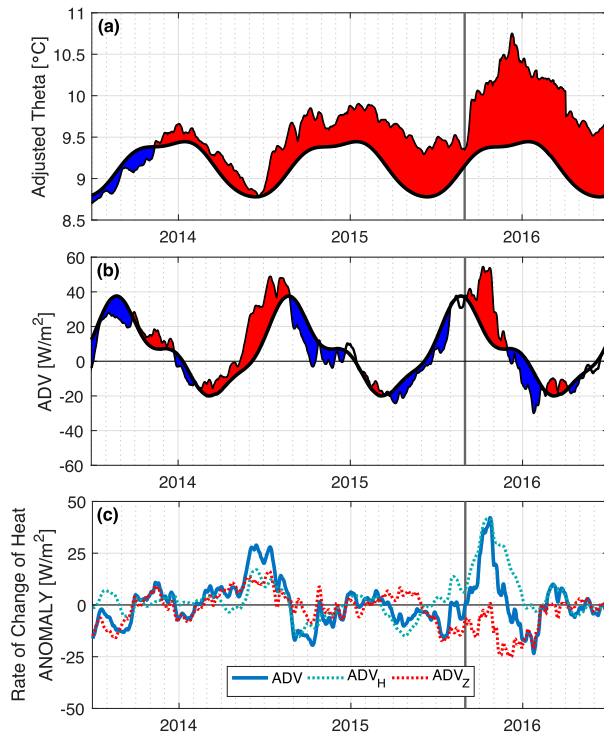
FIG. 13. Time series over 2013.5–16.5 of (a) volume-averaged adjusted potential temperature; also shown are time series of volume-integrated and area-averaged (b) total heat advection and (c) heat advection anomaly. The volume is bound laterally by SBox and vertically by −210- and −100-m depths. In (a) and (b), the thick solid black line is the repeated annual cycle, the thin black line is the interannual signal [unfiltered in (a); filtered with a 3-month running mean in (b)], and the opaque color fill denotes positive (red) and negative (blue) interannual anomalies of 30+-day duration. In (c), the total heat advection (ADV; blue solid) anomaly is decomposed into horizontal (ADV$_H$; turquoise dotted) and vertical (ADV$_Z$; red dotted) components. The gray line is drawn at 1 Sep 2015.

4. Conclusions

Coastal volume and heat budgets are calculated from CASE to diagnose the forcing mechanisms of regional 3D circulation and heat content. The mean volume budgets capture the coastal upwelling overturning cell: its vertical upwelling limb, its shallow cross-shore limb of ageostrophic Ekman transport, and some compensating onshore geostrophic transport (more so in SBox than NBox). At all depths, the mean alongshore geostrophic flow of the CU is convergent in NBox and divergent in SBox. The volume budget exhibits a strong annual cycle, with the strongest upward vertical transport occurring in the spring. The depth-dependent annual cycle of velocity is characterized by upwelling near the surface and downwelling at depth, except during the spring when there is upwelling through the upper 400–500 m of the water column. The dominant terms of the
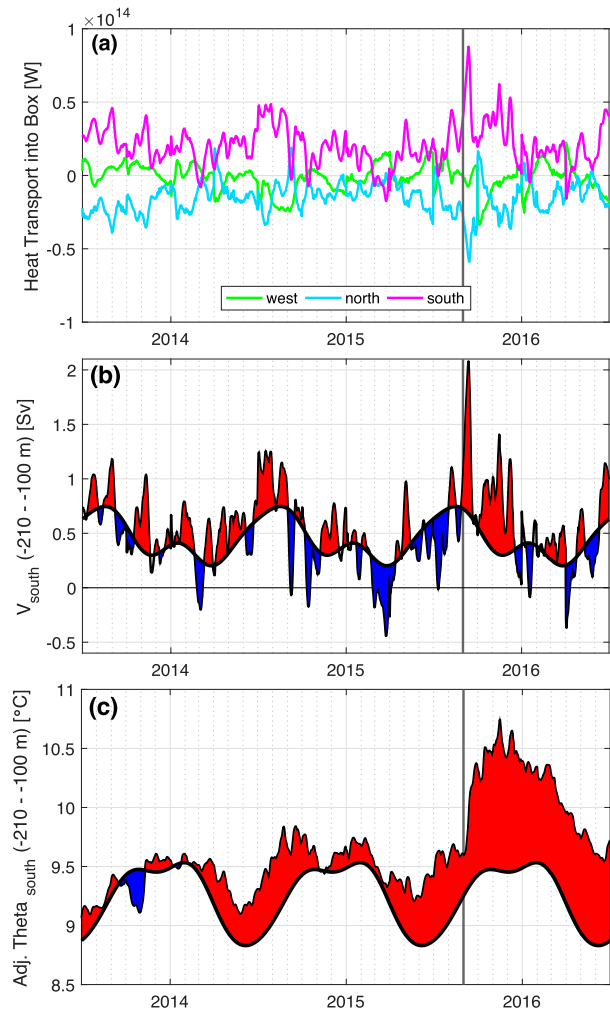

FIG. 14. Breaking apart the −(210–100)-m SBox heat advection term: (a) heat transport across the west (green), north (cyan), and south (magenta) walls (positive is into box), (b) volume transport across the south wall (positive is poleward), and (c) perimeter-averaged adjusted potential temperature along the south wall. In (b) and (c), the thick solid black line is the repeated annual cycle, the thin black line is the interannual signal, and the opaque color fill denotes positive (red) and negative (blue) interannual anomalies of 30+-day duration. The gray line is drawn at 1 Sep 2015.

mean mixed layer heat budgets are downward air–sea heat flux and advective cooling. Their combined contributions drive the total temperature tendency term, which is positive from May to October and negative otherwise. The highest heat storage rate in NBox and SBox occurs in June. Our physical budgets of the mean and annual cycle confirm the classic theories about coastal upwelling circulation, but also provide some new details about the spatial structure and variability of the upwelling overturning cell. Furthermore, they provide a high-resolution baseline against which we can assess interannual budget anomalies.

Interannual budget calculations indicate that multiple forcing mechanisms were relevant during 2014–16, depending on the time and location being examined. The results from our calculations indicate that the upper-ocean heating anomalies from −50 to 0 m in NBox and SBox were driven by intermittent air–sea heat flux and heat advection anomalies. The 2014 air–sea heat flux anomalies have been previously documented (Zaba and Rudnick 2016). They were due to reduced cloud cover (Myers et al. 2018) and a consequent increase in downward solar radiation. Downwelling anomalies persisted throughout most of 2014 and during the upwelling months of 2015. Below average upwelling, and even downwelling during December 2013 and autumn 2014 in NBox, was likely the result of weak coastal winds (Fewings and Brown 2019; Robinson 2016; Zaba and Rudnick 2016). Anomalous alongshore heat advection warmed both volumes from −50 to 0 m in autumn to winter of 2013, as well as NBox in autumn 2014 and SBox in autumn 2015. Anomalous vertical heat advection drove excess potential temperature tendency from summer to autumn 2014. In late 2015, a strong subsurface positive heat advection anomaly was pronounced along the coast, due to an increase in the poleward volume transport and average temperature of the CU. A key takeaway message from our analysis is that there was substantial variability within the huge spatial imprint of the 2014/15 MHW and 2015/16 El Niño warming signals; different forcing mechanisms were relevant at different times and locations throughout the domain.

Our results and previous 2014–16 CCS anomaly attribution studies (Chao et al. 2017; Frischknecht et al. 2017; Myers et al. 2018) are sensitive to model configurations and the geometry of the ocean volume being analyzed. As discussed in Zaba et al. (2018), the 3-month assimilation window used here is shorter than that of a former long-term (2007–10) version of CASE (Mazloff et al. 2014; Todd et al. 2011, 2012; Verdy et al. 2014) to increase model controllability of eddy variability. This 3-month window is longer than that of other CCS modeling studies (Chao et al. 2018; Kurapov et al. 2017; Neveu et al. 2016) to capture the continuous evolution of ocean dynamics over monthly time scales. A shorter assimilation window (on the order of days) would likely result in solutions closer to the data constraints with smaller but more frequent increments. A longer assimilation window (on the order of years) would have less frequent increments but would smooth out short spatiotemporal variability. Similar to the impact of model and assimilation configuration, our budget calculations are sensitive to the definition of a box geometry, including its location, size and depth range. Our choice of box perimeters (NBox and SBox) was intended to encompass key coastal CCS dynamics, including the CU Undercurrent. In previous studies, we identified and characterized the CCS anomalies of 2014–16 (Rudnick et al. 2017a; Zaba and Rudnick 2016; Zaba et al. 2018). The results of these studies motivated the choice of depth ranges (from −50 to 0 m and from −210 to −100 m) as vertical bounds to the shallow and deep warming penetration of the 2014/15 MHW and 2015/16 El Niño, respectively. For any budget calculation, the choices of boundaries in four dimensions matters, and all we can do is be explicit about our choices.

This work presents an analysis over 2014–16 of near-surface circulation and temperature anomalies, as well as the surface heat flux and heat advection anomalies that drove periods of warming. Surface heat flux anomalies have been linked to changes in low cloud cover and downward shortwave radiation (Myers et al. 2018), and vertical downwelling anomalies have been linked to local wind forcing (Fewings and Brown 2019; Zaba and Rudnick 2016) and coastally trapped waves (Frischknecht et al. 2017). Horizontal heat advection anomalies are more difficult to explain, particularly the alongshore component, because they can be influenced by a combination of atmospheric and oceanic conditions both local and remote. Local alongshore heat advection in the coastal margin depends largely on the properties of the California Undercurrent, which are influenced by the variability of: its upstream tropical source water (Pacific Equatorial Water) (Bograd et al. 2019), coastal forcing mechanisms between the tropics and the midlatitude CCS, and local to large-scale alongshore pressure gradients. Future work aimed at understanding the underlying causes of alongshore heat advection anomalies during 2014–16 could include the calculation of CASE's momentum budget or the analysis of basin-scale models or datasets.

REFERENCES

Bograd, S. J., T. K. Chereskin, and D. Roemmich, 2001: Transport of mass, heat, salt, and nutrients in the southern California Current System: Annual cycle and interannual variability. *J. Geophys. Res.*, **106**, 9255–9275, https://doi.org/10.1029/1999JC000165.

——, I. D. Schroeder, and M. G. Jacox, 2019: A water mass history of the southern California Current System. *Geophys. Res. Lett.*, **46**, 6690–6698, https://doi.org/10.1029/2019GL082685.

Bond, N. A., M. F. Cronin, H. Freeland, and N. Mantua, 2015: Causes and impacts of the 2014 warm anomaly in the NE Pacific. *Geophys. Res. Lett.*, **42**, 3414–3420, https://doi.org/10.1002/2015GL063306.

Carton, J. A., G. A. Chepurin, L. Chen, and S. A. Grodsky, 2018: Improved global net surface heat flux. *J. Geophys. Res. Oceans*, **123**, 3144–3163, https://doi.org/10.1002/2017JC013137.

Cavole, L., and Coauthors, 2016: Biological impacts of the 2013–2015 warm-water anomaly in the northeast Pacific: Winners, losers, and the future. *Oceanography*, **29**, 273–285, https://doi.org/10.5670/oceanog.2016.32.

Chao, Y., and Coauthors, 2017: The origins of the anomalous warming in the California coastal ocean and San Francisco Bay during 2014-2016. *J. Geophys. Res. Oceans*, **122**, 7537–7557, https://doi.org/10.1002/2017JC013120.

——, and Coauthors, 2018: Development, implementation, and validation of a California coastal ocean modeling, data assimilation, and forecasting system. *Deep-Sea Res. II*, **151**, 49–63, https://doi.org/10.1016/j.dsr2.2017.04.013.

Chassignet, E. P., H. E. Hurlburt, O. M. Smedstad, G. R. Halliwell, P. J. Hogan, A. J. Wallcraft, R. Baraille, and R. Bleck, 2007: The HYCOM (HYbrid Coordinate Ocean Model) data assimilative system. *J. Mar. Syst.*, **65**, 60–83, https://doi.org/10.1016/j.jmarsys.2005.09.016.

Chereskin, T. K., 1995: Direct evidence for an Ekman balance in the California current. *J. Geophys. Res.*, **100**, 18 261–18 269, https://doi.org/10.1029/95JC02182.

Davis, R. E., 2010: On the coastal-upwelling overturning cell. *J. Mar. Res.*, **68**, 369–385, https://doi.org/10.1357/002224010794657173.

Di Lorenzo, E., and N. Mantua, 2016: Multi-year persistence of the 2014/15 North Pacific marine heatwave. *Nat. Climate Change*, **6**, 1042–1047, https://doi.org/10.1038/nclimate3082.

Eber, L. E., and R. P. Hewitt, 1979: Conversion algorithms for the CalCOFI station grid. CalCOFI Rep. 54, 10 pp.

Edwards, K. A., and K. A. Kelly, 2007: A seasonal heat budget across the extent of the California Current. *J. Phys. Oceanogr.*, **37**, 518–530, https://doi.org/10.1175/JPO2990.1.

Fewings, M. R., and K. S. Brown, 2019: Regional structure in the marine heat wave of summer 2015 off the western United States. *Front. Mar. Sci.*, **6**, 564, https://doi.org/10.3389/fmars.2019.00564.

Frischknecht, M., M. Munnich, and N. Gruber, 2017: Local atmospheric forcing driving an unexpected California Current System response during the 2015-2016 El Niño. *Geophys. Res. Lett.*, **44**, 304–311, https://doi.org/10.1002/2016GL071316.

Gentemann, C. L., M. R. Fewings, and M. Garcia-Reyes, 2017: Satellite sea surface temperatures along the West Coast of the United States during the 2014-2016 northeast Pacific marine heat wave. *Geophys. Res. Lett.*, **44**, 312–319, https://doi.org/10.1002/2016GL071039.

Gómez-Valdivia, F., A. Pares-Sierra, and A. L. Flores-Morales, 2017: Semiannual variability of the California undercurrent along the southern California Current System: A tropical

generated phenomenon. *J. Geophys. Res. Oceans*, **122**, 1574–1589, https://doi.org/10.1002/2016JC012350.

Jacox, M. G., E. L. Hazen, K. D. Zaba, D. L. Rudnick, C. A. Edwards, A. M. Moore, and S. J. Bograd, 2016: Impacts of the 2015-2016 El Niño on the California Current System: Early assessment and comparison to past events. *Geophys. Res. Lett.*, **43**, 7072–7080, https://doi.org/10.1002/2016GL069716.

Kalnay, E., and Coauthors, 1996: The NCEP/NCAR 40-Year Reanalysis Project. *Bull. Amer. Meteor. Soc.*, **77**, 437–471, https://doi.org/10.1175/1520-0477(1996)077<0437:TNYRP>2.0.CO;2.

Kurapov, A. L., N. A. Pelland, and D. L. Rudnick, 2017: Seasonal and interannual variability in along-slope oceanic properties off the US West Coast: Inferences from a high-resolution regional model. *J. Geophys. Res. Oceans*, **122**, 5237–5259, https://doi.org/10.1002/2017JC012721.

Large, W. G., and S. Pond, 1981: Open ocean momentum flux measurements in moderate to strong winds. *J. Phys. Oceanogr.*, **11**, 324–336, https://doi.org/10.1175/1520-0485(1981)011<0324:OOMFMI>2.0.CO;2.

Lynn, R. J., and J. J. Simpson, 1987: The California Current System: The seasonal variability of its physical characteristics. *J. Geophys. Res.*, **92**, 12 947–12 966, https://doi.org/10.1029/JC092iC12p12947.

——, and S. J. Bograd, 2002: Dynamic evolution of the 1997-1999 El Niño-La Niña cycle in the southern California current system. *Prog. Oceanogr.*, **54**, 59–75, https://doi.org/10.1016/S0079-6611(02)00043-5.

Marshall, J., A. Adcroft, C. Hill, L. Perelman, and C. Heisey, 1997: A finite-volume, incompressible Navier Stokes model for studies of the ocean on parallel computers. *J. Geophys. Res.*, **102**, 5753–5766, https://doi.org/10.1029/96JC02775.

Mazloff, M. R., S. T. Gille, and B. Cornuelle, 2014: Improving the geoid: Combining altimetry and mean dynamic topography in the California coastal ocean. *Geophys. Res. Lett.*, **41**, 8944–8952, https://doi.org/10.1002/2014GL062402.

McCabe, R. M., and Coauthors, 2016: An unprecedented coastwide toxic algal bloom linked to anomalous ocean conditions. *Geophys. Res. Lett.*, **43**, 10 366–10 376, https://doi.org/10.1002/2016GL070023.

Myers, T. A., C. R. Mechoso, G. V. Cesana, M. J. DeFlorio, and D. E. Waliser, 2018: Cloud feedback key to marine heatwave off Baja California. *Geophys. Res. Lett.*, **45**, 4345–4352, https://doi.org/10.1029/2018GL078242.

Nelson, C. S., 1977: Wind stress and wind stress curl over the California Current. NOAA Tech. Rep. NMFS SSRF-714, 87 pp., NTIS PB-272310, https://spo.nmfs.noaa.gov/sites/default/files/legacy-pdfs/SSRF714.pdf.

Neveu, E., A. M. Moore, C. A. Edwards, J. Fiechter, P. Drake, W. J. Crawford, M. G. Jacox, and E. Nusse, 2016: An historical analysis of the California Current circulation using ROMS 4D-Var: System configuration and diagnostics. *Ocean Modell.*, **99**, 133–151, https://doi.org/10.1016/j.ocemod.2015.11.012.

Paulson, C. A., and J. J. Simpson, 1977: Irradiance measurements in upper ocean. *J. Phys. Oceanogr.*, **7**, 952–956, https://doi.org/10.1175/1520-0485(1977)007<0952:IMITUO>2.0.CO;2.

Robinson, C. J., 2016: Evolution of the 2014-2015 sea surface temperature warming in the central west coast of Baja California, Mexico, recorded by remote sensing. *Geophys. Res. Lett.*, **43**, 7066–7071, https://doi.org/10.1002/2016GL069356.

Rudnick, D. L., K. D. Zaba, R. E. Todd, and R. E. Davis, 2017a: A climatology of the California Current System from a network

of underwater gliders. *Prog. Oceanogr.*, **154**, 64–106, https://doi.org/10.1016/j.pocean.2017.03.002.

——, ——, ——, and ——, 2017b: A climatology using data from the California Underwater Glider Network. Scripps Institution of Oceanography, Instrument Development Group, accessed 6 April 2017, https://doi.org/10.21238/S8SPRAY7292.

Rykaczewski, R. R., and D. M. Checkley, 2008: Influence of ocean winds on the pelagic ecosystem in upwelling regions. *Proc. Natl. Acad. Sci. USA*, **105**, 1965–1970, https://doi.org/10.1073/pnas.0711777105.

Stammer, D., and Coauthors, 2002: Global ocean circulation during 1992-1997, estimated from ocean observations and a general circulation model. *J. Geophys. Res.*, **107**, 3118, https://doi.org/10.1029/2001JC000888.

Talley, L. D., G. L. Pickard, W. J. Emery, and J. H. Swift, 2011: Pacific Ocean. *Descriptive Physical Oceanography*, Academic Press, 303–362.

Tamsitt, V., L. D. Talley, M. R. Mazloff, and I. Cerovecki, 2016: Zonal variations in the Southern Ocean heat budget. *J. Climate*, **29**, 6563–6579, https://doi.org/10.1175/JCLI-D-15-0630.1.

Todd, R. E., D. L. Rudnick, M. R. Mazloff, R. E. Davis, and B. D. Cornuelle, 2011: Poleward flows in the southern California Current System: Glider observations and numerical simulation. *J. Geophys. Res.*, **116**, C02026, https://doi.org/10.1029/2010JC006536.

——, ——, ——, B. D. Cornuelle, and R. E. Davis, 2012: Thermohaline structure in the California Current System: Observations and modeling of spice variance. *J. Geophys. Res.*, **117**, C02008, https://doi.org/10.1029/2011JC007589.

Valdivieso, M., and Coauthors, 2017: An assessment of air-sea heat fluxes from ocean and coupled reanalyses. *Climate Dyn.*, **49**, 983–1008, https://doi.org/10.1007/s00382-015-2843-3.

Verdy, A., M. R. Mazloff, B. D. Cornuelle, and S. Y. Kim, 2014: Wind-driven sea level variability on the California coast: An adjoint sensitivity analysis. *J. Phys. Oceanogr.*, **44**, 297–318, https://doi.org/10.1175/JPO-D-13-018.1.

Zaba, K. D., and D. L. Rudnick, 2016: The 2014-2015 warming anomaly in the Southern California Current System observed by underwater gliders. *Geophys. Res. Lett.*, **43**, 1241–1248, https://doi.org/10.1002/2015GL067550.

——, ——, B. D. Cornuelle, G. Gopalakrishnan, and M. R. Mazloff, 2018: Annual and interannual variability in the California current system: Comparison of an ocean state estimate with a network of underwater gliders. *J. Phys. Oceanogr.*, **48**, 2965–2988, https://doi.org/10.1175/JPO-D-18-0037.1.